Laboratory Measurement of the DInSAR Response to Spatiotemporal Variations in Soil Moisture

Keith Morrison, *Member, IEEE*, John C. Bennett, Matt Nolan, and Raghav Menon

***Abstract*—Differential interferometric synthetic aperture radar (DInSAR) has traditionally been used for the detection and accurate monitoring of surface movement in a scene and has found applications in fields such as mining subsidence and earthquake deformation. In these studies, the phase is understood to directly relate to the radial component of the physical deformation of the surface. In this paper, however, we use a novel combination of microwave and optical laboratory measurements to demonstrate the presence of persistent and coherent phase changes in a temporal sequence of DInSAR images, related solely to moisture change in a soil. This is confirmation of recent reports suggesting that, in some circumstances, the DInSAR signal may include a significant soil moisture signal. Laboratory measurements were used to obtain a set of high-resolution C-band DInSAR images of a sandy soil sample of an area of 2.0 m $\times$ 1.8 m and a depth of 0.2 m, with the fractional volumetric water content varying between 0.1 and 0.4. To independently monitor the soil surface for physical movement, a time-lapsed set of high-resolution digital optical images was continuously acquired. Although the soil underwent a large moisture change, the soil surface was static to within $\pm$0.1 mm over the majority of the experiment. The DInSAR sequence displayed dynamic and complex variations of the phase, although a linear relationship with moisture change was evident when the mean phase change was considered. The work raises the possibility that DInSAR could be used for the monitoring of soil moisture change in a scene, a parameter of significant economic and environmental importance.**

***Index Terms*—Differential interferometric synthetic aperture radar (DInSAR), ground-based SAR (GB-SAR), interferometry, soil moisture.**

I. Introduction

SOIL moisture is a key environmental parameter which plays a primary role in regional and global climate dynamics and has significant economic importance [1]–[4], yet its reliable measurement at spatial scales of less than a kilometer has remained elusive. An ability to accurately map soil moisture could also provide significant help in support of hydrological and flood planning and civil engineering activities, which is not currently available. Knowledge of soil moisture at resolutions of meters is practically impossible on the ground by field measurements, and a viable remote-sensing technique to do so has remained unidentified [5]. Field measurements are plagued not only by inadequate measurement techniques and the enormous man-power requirements for large studies but also by difficulties in scaling point measurements to larger areas [6].

Nearly all prior microwave studies of soil moisture have only utilized the amplitude information in synthetic aperture radar (SAR) imagery, rather than the phase, with multipolarization techniques perhaps showing the most promise [7]–[9]. However, there is mounting evidence that differential interferometric SAR (DInSAR) is responsive to soil moisture. Gabriel *et al.* [10] likely first reported the presence of spatial inhomogeneities in soil moisture through the interferometric phase signal, using L-band Seasat differential interferograms over farmland which showed strong correlations between the phase and field boundaries. It was proposed that the phase signals could be interpreted through the shrink/swell of the clay soils. However, ground-truth surface elevation measurements were not taken, and the hypothesis remained to be confirmed. Later, C-band studies have also suggested phase variations across farmland associated with the physical movement of the soil horizon through shrink/swell [11]–[13] but, again, without ground-truth confirmation. The most quantitative investigation to date of a phase–soil moisture signal link was made in [14]. They used C-band European Remote Sensing satellite ERS-2 imagery of both cultivated and uncultivated regions in a high-plains area of Colorado, in combination with ground-based moisture measurements. The DInSAR imagery showed millimeter-scale path-length changes. Clay soils can be expected to exhibit shrink/swell with moisture variations [15]. While they showed a strong correlation between hydrological features such as stream channels and watershed boundaries and the differential phase, they were unable to conclusively demonstrate a link between the differential phase and soil moisture effects.

Clearly, these studies have shown that a soil moisture signal has the potential to be a source of significant error in DInSAR land deformation analysis. Additionally, it holds the promise that, in some instances, the phase signature may be a proxy for soil moisture, with all the attendant benefits that such a relationship could bring in remote sensing techniques. In an attempt to unambiguously confirm the presence or not of a moisture signal in DInSAR, this paper reports on the results of a detailed and controlled laboratory study of a soil sample with varying moisture content.

Manuscript received April 12, 2010; revised October 5, 2010 and February 2, 2011; accepted March 3, 2011. Date of publication April 28, 2011; date of current version September 28, 2011. This work was supported by the U.S. Department of Defense through the Army Research Laboratory's Defense Experimental Program to Stimulate Competitive Research program.

K. Morrison and R. Menon are with the Department of Informatics and Systems Engineering, Cranfield University, SN6 8LA Swindon, U.K. (e-mail: k.morrison@cranfield.ac.uk; r.menon@cranfield.ac.uk).

J. C. Bennett is with the University of Sheffield, S1 3JD Sheffield, U.K. (e-mail: j.c.bennett@sheffield.ac.uk).

M. Nolan is with the Institute of Northern Engineering, University of Alaska at Fairbanks, Fairbanks, AK 99775 USA (e-mail: matt@drmattnolan.org).

Digital Object Identifier 10.1109/TGRS.2011.2132137

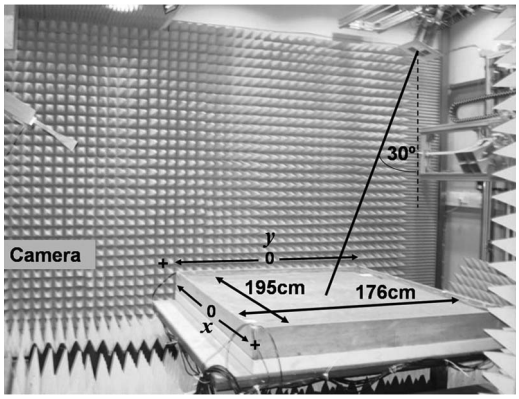

Fig. 1. Imaging scheme, showing the soil sample positioned in the anechoic chamber in its measurement position. Part of the planar ceiling-mounted scanner is visible at the top right. The line indicates the 30° incidence angle from the antennas to the center of the sample. The position of the camera is also indicated, which was just off the picture. The $x - y$ coordinate system is displayed, where x lies along the cross-range direction and y is along the range direction. The system is defined such that $x = 0$, $y = 0$ lies at the center of the soil sample, and the positive directions from zero are indicated.

II. Experimental Scheme

A program of experimental work was undertaken at the indoor ground-based SAR (GB-SAR) microwave measurement facility [16]. This is a 6 m $(l) \times 4$ m $(w) \times 3$ m (h) anechoic chamber and is shown in Fig. 1 with the soil sample *in situ*. The chamber provides a highly controlled radar measurement environment. The 2-D ceiling-mounted planar scanner used in the measurements can be seen at one end of the chamber. This is moved under computer control and provides repeatable high-precision positioning. Fig. 1 shows the soil sample in its measurement position, contained within a 1.8 m $\times$ 2.0 m $\times$ 0.25 m trolley-mounted box. The box has wooden sides and an impermeable Perspex base. Radar measurement of the sample was carried out on Days 1, 9, 16, 24, 30, 37, and 50 over the 50-day period with decreasing volumetric water content (VWC) m_v. By careful control of the measurements, this was the only free parameter, allowing a quantitative investigation of the temporal response of the DInSAR phase to varying moisture.

A. Soil Sample

A 100% fine sandy loam sample was used in the measurements, with negligible ($< 0.5\%$) clay content. It had a dry-weight density of 1.602 g/cm^3. It was added to the trolley box to produce a sample with dimensions of 176 cm (range) $\times$ 195 m (cross-range), as shown in Fig. 1. The mean sand depth was 20.5 cm, providing a total volume of 0.70 m^3. It was raked during in-filling to provide homogeneity across and through the sample. Eight Campbell Scientific CS615 moisture probes were installed through the vertical soil volume in a staggered arrangement to avoid vertical alignment between probes. The top two were 2 cm below the surface on opposite corners of the box. Four were placed at a mid-depth of 10 cm alongside the center of each box face. Finally, the remaining two were positioned 18 cm down, 2 cm above the base of the soil, at opposite corners to those used for the top probes. All were installed around the edge of the box, with their rods horizontal and parallel to the box edges. Although the depth and positioning of the probes in the vicinity of the box wall is not the ideal deployment, this was regarded as a necessary compromise to avoid any possible clutter contamination of the radar measurements over the central soil area. The probes provided hourly readings to a Campbell Scientific CR1000 data logger during the course of the experiment. The trolley was locked in position to ensure that no movement disturbance occurred to the sample during the experiment.

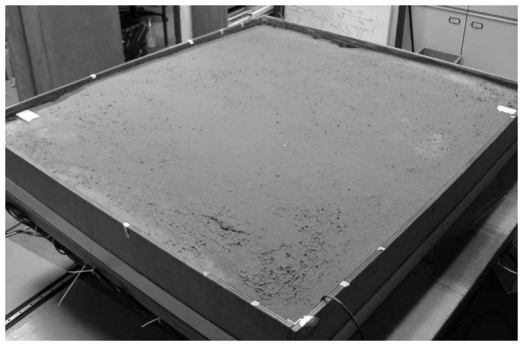

Fig. 2. Soil sample on Day 1 of the measurements, two days after watering. The two white rectangular features visible at opposite corners of the sample are parts of the two top-positioned soil moisture probes.

At the start of the experiment, water was added to the surface directly from a watering can. With knowledge of the mean initial moisture content from the meter readings, the necessary water was added to bring the VWC up to the required 0.4 fractional (40%) starting level. Some transient pooling of the water occurred, with some slight pitting and cracking at the edges of the sample, either outside or on the edge of the radar area of interest. Fig. 2 shows the sand two days after wetting, on Day 1 of the measurements. The sand appears very smooth in the central area, and the point features just visible across the surface correspond to small ~ 0.5 cm $\times$ 0.5 cm pebbles, which were present in the soil at $\ll$1% by volume. The measurements relied on slow drying of the sample within the 15 °C–20 °C air-conditioned laboratory. The expected performance figures for the probes provided by the manufacturers indicate an absolute accuracy for VWC measurement with the CS615 probes of 2%. Testing of the probes in air and water (VWC of 0% and 100%, respectively) always gave readings within 5% but, more usually, within 3%.

B. Radar Measurements

A series of repeat SAR imaging scans of the soil sample were made from the scanner, with an exact spatial repeat. The target and antenna were positioned such that the center of the soil sample was viewed at an incidence angle of 30° from the center of the scan aperture, as indicated in Fig. 1. Because of the proximity of the antennas and the sample, the incidence angle varied significantly across the sample. All measurements were C-band VV polarization.

The microwave RF subsystem is based around an HP8720DX vector network analyzer. The spacing of the samples along the aperture dx was set at 1.5 cm $(\lambda/4)$ so as to avoid grating lobes. During imaging, the antenna stopped at

each sample point along the aperture, stepped through a set of 401 spot frequencies at 5-MHz intervals over a 4–6-GHz bandwidth, then moved on dx, and repeated the process until 77 samples had been collected over a 114-cm aperture. Thus, an image is not collected instantaneously but takes 1.5 min during which time RF and mechanical stability of the radar and target must be maintained. Each scan provides a complex single-look SAR image. The antennas were 200 cm above the soil surface and displaced 116 cm from the center of the sample, providing an incidence angle to the center of the box of 30°. The SAR "antenna" actually consists of a pair of identical transmit and receive pyramidal horn antennas with dimensions of 8.0 cm $(w)\times$ 10.0 cm (h), with an offset which is sufficiently small to allow the data to be processed as if they were a single monostatic antenna. Stringent calibration procedures were required for the radar measurements, which used a methodology based on [17]. A reference sphere with precisely known scattering characteristics was used to correct for system effects and to provide an absolute calibration of the data.

C. Optical Imaging

In order to correctly interpret the radar measurements, it was necessary to optically monitor the sample for any physical movement of the surface horizon during the experiment. For this purpose, high-resolution (2448 × 3264 pixel) digital color photographs of the soil were acquired using an Olympus SP-350 digital camera. A time-lapse series of photographs at 99-min intervals was recorded over almost the entire 50-day duration of the experiment. The camera was installed 1.55 m to the rear of the sample, as indicated in Fig. 1. As we were primarily interested in measuring the vertical change in the soil surface, maximum accuracy was provided by observing from a shallow angle. However, some obliqueness to the surface was required to provide good separation in range of the surface features and avoid obscuration. The camera angles to the front and rear of the sample were 73° and 82°, respectively.

Because of the low contrast and lack of discernable features over the soil surface, markers were added which could more easily be tracked. The markers had to be small and light enough so as not to cause any local disturbance to the soil surface or trap moisture below them and give false effects. Small expanded polystyrene balls with a diameter of typically 4 mm were selected, of the type normally used as cushion fill. Being white, they provided a good contrast with the soil surface. Fig. 3 shows a photograph of the soil sample, with the white markers clearly visible. The two balls marked with the arrow are shown expanded over a 60 × 90 pixel region on the left of the figure. The larger of the balls was 5.43 mm in diameter and appears 23 pixels high in the image such that each pixel represents 0.24 mm.

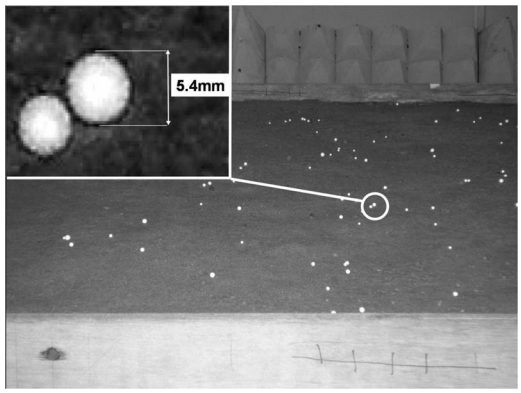

Fig. 3. Camera's view of the soil sample, showing the distribution of polystyrene marker balls across the surface. The inset shows a 60 × 90 pixel zoomed view of the two markers indicated.

TABLE I
SUMMARY OF IMAGE PARAMETERS INCIDENCE ANGLE, RANGE, AND CROSS-RANGE RESOLUTION ACROSS THE SOIL SAMPLE ON BORESIGHT (FROM APERTURE CENTER DOWN SOIL CENTERLINE)

Position	i^o (degrees)	Range (cm)	Cross-Range (cm)
Near Box Edge	8	70	7
Box Centre	30	20	8
Far Box Edge	45	14	10

III. Data Processing

A. SAR Imagery

A synthetic-pulse plane-to-plane imaging scheme was used to construct the time series of SAR images [18], [19]. The reconstruction process presents the images in ground range in an image plane at the height of the soil surface, 200 cm below the antennas. This preserved the positional relationship that it had in the chamber relative to the antennas. The image pixel size is 1.5 cm × 1.5.cm. The resolution changes across the image. The range resolution Res_R is given by

$$\mathrm{Res}_R = W\frac{c}{2B\sin i} \tag{1}$$

where c is the speed of light, i is the incidence angle, B is the bandwidth (2 GHz), and W accounts for windowing of the data (1.3 for a Hamming window). Thus, the range resolution in an image varies depending upon the local incidence angle. As a result, the range resolution is very poor at the near box edge because the angle of incidence here is only about 8°. The cross-range resolution Res_{XR} is given by

$$\mathrm{Res}_{XR} = W\frac{\lambda R}{2D\cos\xi} \tag{2}$$

where $\lambda =$ wavelength, $R =$ slant range, $D =$ aperture length (114 cm), and ξ is the angle away from the boresight (image range centerline). The image resolutions are summarized in Table I and were 20 and 8 cm in range and cross-range, respectively, at the center of the sample. An example SAR amplitude image from Day 1 is shown in Fig. 4. It is not corrected for space loss, antenna beam pattern, or processing gains. This is not necessary as these were constant for each image, and we are only interested in the retrieval of the phase. An outline of the soil sample is indicated by the rectangular white line. The reduced resolution at the near range due to the steep incidence angle is evident from the backscattering pattern. The feature

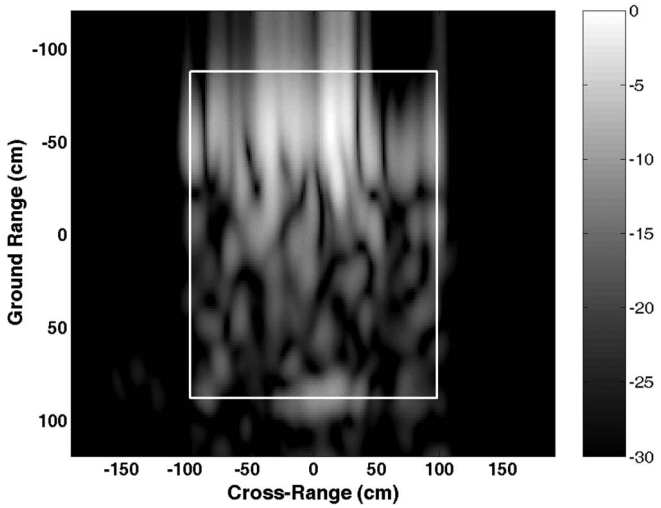

Fig. 4. SAR image of the soil sample obtained on Day 1, displayed over a 30-dB range. The 176 cm $\times$ 195 cm outline of the sample is indicated by the white rectangle.

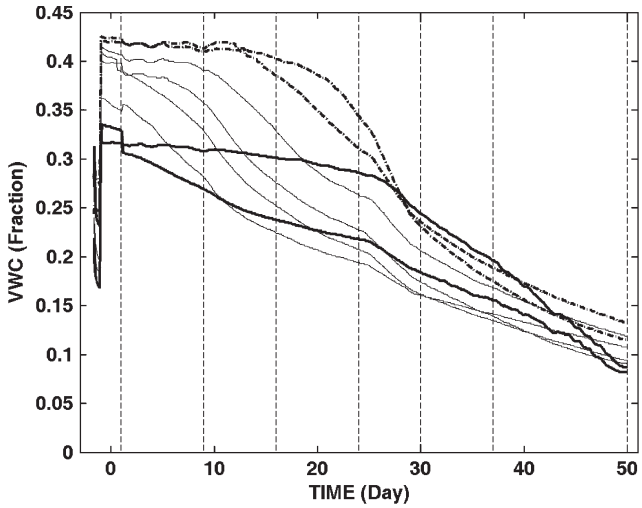

Fig. 5. Temporal variation of VWC m_v measured at the soil moisture probes over the course of the experiment. The top two probes are indicated by the solid thick lines, the four middle probes by the thin solid lines, and the two bottom probes by the thick dashed-dotted lines. The vertical lines mark each of the seven measurement days.

along the center of the far-range limit of the sample is a double bounce return from the soil and box edge.

These measurements posed some special problems because of the need to have no disturbance to the experimental setup once the measurements began such that the calibration had to be carried out prior to the experiment. In a measurement program of this type, where changes in phase were to be measured accurately, it was vital to correct for any drift of the RF subsystem over the experiment interval. To do this, the GB-SAR system continuously monitored the signal directly coupled between the transmit and receive antennas, which contains information relating to all the amplitude and phase variations present in the complete hardware path from transmitter to receiver, while excluding external signals. This technique has previously been successively employed to correct for system drift for long-duration imaging and is described in more detail in [20]. With this scheme, it was possible to apply the calibration at any point in time over the duration of the experiment, with a confidence of better than 2°.

B. VWC Variation

The variation of VWC over the course of the experiment is shown in Fig. 5. The jump in VWC is very apparent at the start of the measurements. A smaller jump on Day 1 corresponds to the first entry into the chamber since the addition of the water two days earlier and an increase in ventilation. VWC was seen to fall continuously at all sensors from around 0.4 to 0.1 over the seven weeks. There is clearly some spatial variability in the 3-D moisture profile, which was largest between the measurement Days 9 and 24, when it was as large as 0.18. At the end of the measurements, the spread in moisture was smallest at 0.05. There was also some redistribution of the moisture ratios between different probes over the course of the work, leading to a variable vertical moisture gradient during the measurements. As might be expected, the two bottom sensors recorded the highest moisture values, and the top sensors recorded generally the lowest. One of the two top-placed sensors appears anomalous in that it cuts across the profiles of the other probes, going from the lowest to the highest VWC and then going almost to the lowest again. Particularly because of the large differences between the top two probes, in the analysis, we choose to use mean values of m_v averaged across all sensors. The use of a "bulk" value is justified as it likely has more relevance to real-world measurements and applications, and Fig. 5 shows that there is a strong correlation between the behavior of m_v at different depths measured by the probes.

C. Optical Displacement Tracking

By stitching the time-lapse photographs together, a movie was produced, which could be zoomed to produce a very high resolution inspection of the temporal displacement behavior of any part of the photographed soil surface. Because the target and camera were unmoved during the experiment, tracking the positional history of the soil markers provides the vertical displacement history of the soil. As the number of markers in an image is large (93) and the number of images is even larger (599), an automated technique was developed to perform the analysis. A mask was first applied to the image to exclude regions that are not of interest, namely, the box edges and everything outside. To remove random "salt and pepper" noise, the image was median filtered with a 10 $\times$ 10 window. The markers were bright against the soil, and their separation from the background relied on level thresholding. The images were integer 256, and a level $>$175 was found to be optimum in terms of marker detection against false alarms. Additionally, the images were separated out into their component red-green-blue (RGB) images for further improvement in marker discrimination. As white corresponds to equal contributions from each RGB image, the combined thresholding was applied across the component images. The technique calculates a center of mass, or centroid, C

$$C(p,q) = \frac{\sum c_{ij} A_{ij}}{\sum c_{ij}} \tag{3}$$

where ij refers to the horizontal and vertical pixel coordinates, respectively, A is the weighting factor given by the amplitude value at a pixel, and p and q give the specific point at which the total mass of the system appears to be concentrated for each marker.

To convert vertical movement into a real height change, the next step involved deriving a spatial scaling function across the image, $V(p, q)$. For a given vertical movement, the movement in pixels seen by the camera will vary across the scene due to changes in viewing geometry and optical resolution. The function V captures this information and converts movement in pixels at each marker position into an absolute estimate in millimeters of the local vertical movement Δh between frames m and n, where only the change in the vertical coordinate q is considered

$$\Delta h = [C_n - C_m]_q V. \tag{4}$$

IV. Results

A. DInSAR Phase Behavior

A series of complex SAR images was constructed for each of the measurement days. Using the first week as the master I_1, a series of complex differential interferograms D_{1_N} was constructed by reference against successive images I_N pixel by pixel

$$D_{1\_N} = angle\left\{\frac{I_1}{|I_1|}.\frac{I_N^*}{|I_N|}\right\} \tag{5}$$

where $N = 9$, 16, 24, 30, 37, and 50. Fig. 6 shows the spatial development of the differential phase with time across the central 1.5 m $\times$ 1.5 m region of the sample during the course of 50 days. It displays $D_{1\_9}, D_{1\_16}, \ldots D_{1\_50}$ successively from top to bottom, each over a $\pm 180^\circ$ dynamic range. The analysis uses the convention that negative values correspond to increasing path length between the radar and target.

The spatial behavior of D_{1_N} is complex at these high resolutions but exhibited a smooth and consistent development, with temporally coherent features between interferograms. The final image D_{1_50} is much less consistent, presumably due to the very dry conditions of $m_v = 0.10$ and larger time step relative to the previous measurement intervals. All images display features showing both positive and negative phase excursions. However, it is evident from their time development that most of the positive excursions can be understood as phase wraparound from an initially negative excursion. The bright 95-pixel region A can be continuously traced back in time to a developing feature evident in D_{1_9}. It shows a continuously increasing negative phase, which first displays wraparound in D_{1_24}. The average D_{1_9} to D_{1_37} phase behavior is displayed in Fig. 7 plotted against Δm_v, where Δm_v represents the change in m_v relative to the first measurement on Day 1

$$\Delta m_v = m_{v,N} - m_{v,1} \tag{6}$$

and $N = 9$, 16, 24, 30, and 37. The difference between a quadratic and a linear fit was small, and a linear fit

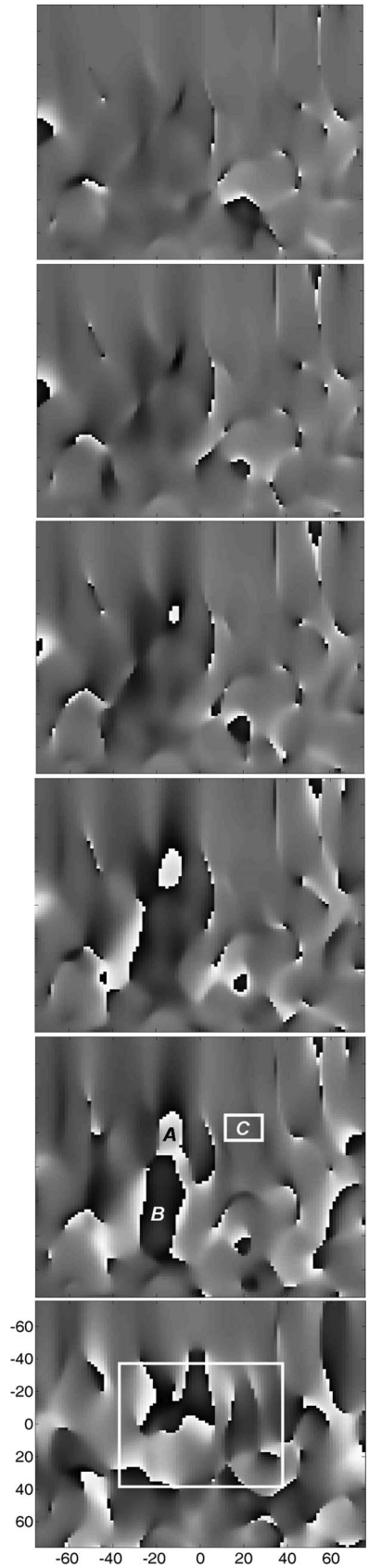

Fig. 6. Differential phase images. (From the top) $D_{1\_9}, D_{1\_16}, D_{1\_24}, D_{1\_30}, D_{1\_37}, D_{1\_50}$. Each 150 cm $\times$ 150 cm plot is displayed over a $\pm 180^\circ$ dynamic range. The 75 cm $\times$ 75 cm area used in the histogram analysis is displayed over the D_{1_50} plot. Regions A, B, and C are indicated in D_{1_37}.

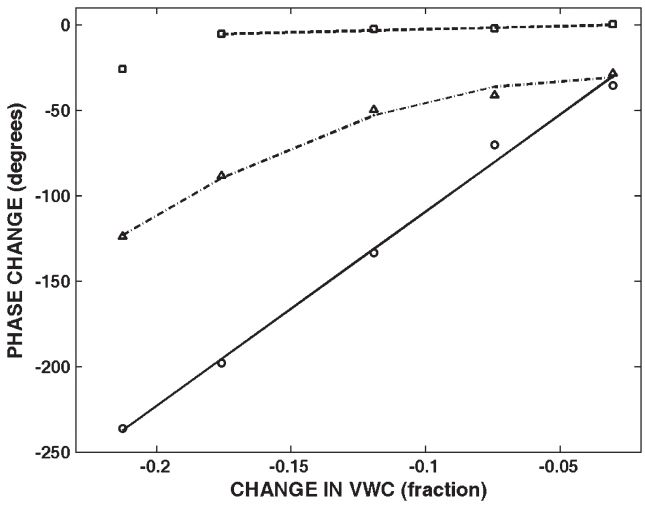

Fig. 7. Variation of phase for the regions highlighted in D_{1_37} in Fig. 6 against change in VWC. The circles show the measured phase in region A, and the solid line is a linear fit $y = 1137\Delta m_v - 4$. The triangles are the results for region B, and the dash-dotted line is the quadratic fit $y = -2744\Delta m_v^2 - 160\Delta m_v - 33$. The squares show the fit to the "background" region C, and the dashed line is the linear fit to the first four points $y = 36\Delta m_v - 1$.

$y = 1137\Delta m_v - 4$ was adopted, where y is in degrees. This indicates an average phase change of -11.4° for each 1% decrease in m_v (where Δm_v is negative for a decrease). The phase behavior of the dark 315-pixel region B is also displayed in Fig. 7. It showed a continuous shift to negative values, but with an improved fit with a quadratic over the linear case. The linear fit indicated an average rate of change just under half that in region A, at -5.1° per 1% decrease in m_v. Not all the soil displays such obvious phase changes. The "background" 121-pixel region C highlighted in the D_{1_37} image showed only subtle changes, with a slow drift toward negative values, albeit with a large jump at D_{1_37}. Over D_{1_9} to D_{1_30}, the phase change was linear, corresponding to only -0.4° per 1% decrease in m_v.

Fig. 8 plots the histogram of the frequency of occurrence of the phase distribution, restricted to the central 0.75 m $\times$ 0.75 m to obtain the response close to 30° and reduce possible incidence angle effects. The histograms show a nonsymmetrical temporal development of the phase, increasingly skewed toward more negative values. There is evidence for a multipeaked distribution, most obvious for D_{1_24}. Between D_{1_9} and D_{1_24}, there is a strong return centered on 0°, which becomes increasingly displaced for D_{1_30} and D_{1_37}. In addition to this peak, there is another distribution which appears to break away from zero, moving at a more rapid pace toward negative values and becoming more flattened as it does. By D_{1_30}, the leading tail of the distribution has passed through -180°, producing an obvious wraparound at the positive high end. D_{1_50} has an almost flat phase distribution. However, because of the dry conditions during the final D_{1_50} measurement, we strongly suspect that there was significant penetration through the soil and reflection from the underlying box and trolley, also confirmed by the change in the amplitude pattern. As such, D_{1_50} was not considered in the temporal sequence with the other interferograms.

To obtain the best estimate of the temporal "bulk" phase change, a spatial average was taken over the central 150 cm $\times$ 150 cm soil area. A positive phase between 90° and 180° was assumed to be wrapped and unwrapped by subtracting -360° before the estimation of the mean phase. The result is shown in Fig. 9. The relationship appeared strongly linear, and a best linear fit is shown, with $y = 256\Delta m_v - 12$, indicating a change of 2.6° per 1% change in m_v. From the physical process that the equation represents, as $\Delta m_v \to 0$, we would expect the line to pass through the origin, so the 12° intercept offset is significant and not easily explained, unless the linearity breaks down at very small Δm_v.

B. Optical Height Record

In contrast to the radar results, the optical results indicated very little change in the soil surface. Fig. 10 is a record of the mean displacement during the experiment, and the error bars indicate the standard deviation. The timing of the points corresponds to the mean measurement time of each sequence of images, which generally corresponds to the central interval between radar measurement days. Each time-lapsed block of images was processed separately to provide a mean estimate of motion over that interval, as accessing the images to download involved manual disturbance to the camera, which could have caused subsequent image offsets. Over the first 37 days, i.e., up to the penultimate measurement day, the mean displacement had been measured at less than ± 0.1 mm. This measurement was consistent over the whole soil surface. We can state that, in essence, *no physical movement of the surface horizon* was observed over the first 37 days of the experiment. Between Day 37 and Day 50, there was indication of a -0.9-mm sinking of the surface, only relevant for D_{1_50}. A ± 0.1-mm change would have produced only a maximum phase change of $\pm 1^\circ \cos i$, for a path solely through free space, compared to the observations exceeding 180° in places.

V. Discussion

Normally, for repeat-pass satellite imagery, the DInSAR phase is a summation of various sources

$$\Phi = \Phi_{diff} + \Phi_{topo} + \Phi_{atmos} + \Phi_{noise} \tag{7}$$

where Φ_{diff} is the desired differential phase. The topographic phase Φ_{topo} results from the path difference arising from observing a point from opposite ends of an InSAR baseline, differential extinction Φ_{atmos} from a variable atmospheric contribution, and a noise contribution Φ_{noise} which can arise from various sources such as poor signal to noise. Because the placement of the target and antennas was unchanging and from the close proximity of the radar and target and good signal to noise, we could construct zero-baseline InSAR pairs and interpret the temporal phase change between images directly as Φ_{diff}, where it is assumed a correction has been made for system phase drift. If we make a conventional interpretation of the DInSAR phase, then it arises purely from the apparent change in the radial path Δr to any point in the image. Defining

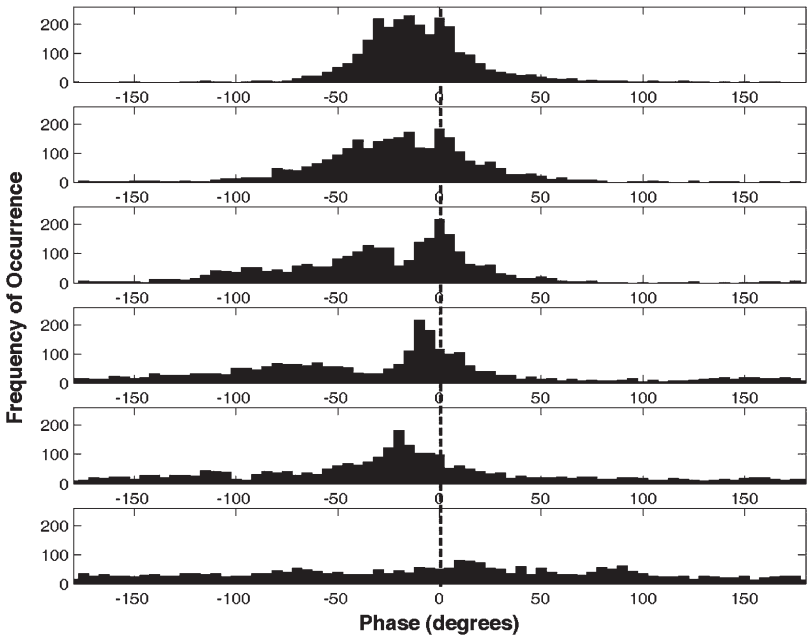

Fig. 8. Histogram of the phase distribution at each pixel over the central 75 cm × 75 cm for (top to bottom) $D_{1\_9}, D_{1\_16}, D_{1\_24}, D_{1\_30}, D_{1\_37}, D_{1\_50}$. Each plot is shown on the same scale and over a $\pm 180^\circ$ range.

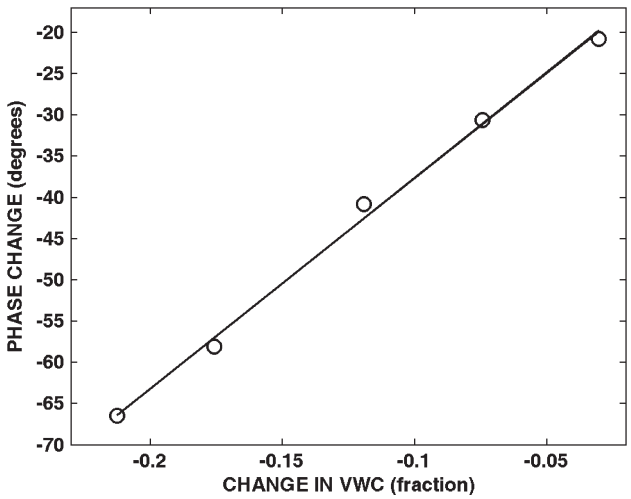

Fig. 9. Bulk differential phase behavior over the central 150 cm × 150 cm of the soil sample. The line is the best linear fit, with $y = 256\Delta m - 12$.

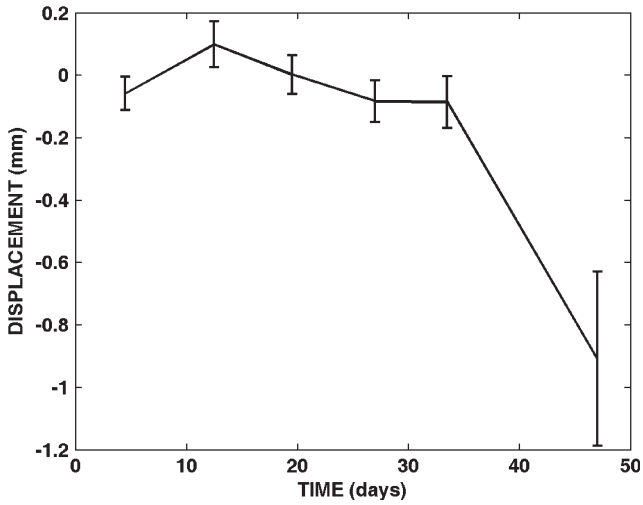

Fig. 10. Mean vertical displacement measured for the soil surface derived from the ball markers over the course of the experiment.

k as the wavenumber in degrees, $k = 360/\lambda$, where λ is the free-space wavelength, it follows that $\Phi_{diff} = 2k\Delta r$ such that

$$\Delta h = \frac{\Phi_{diff}}{2.k.\cos i} = \frac{\Delta r}{\cos i} \tag{8}$$

where Δh is the change in vertical height. The radar only measures a projection of the vertical movement along the radial, and a correction for this is made through the $\cos i$ term, where i is the local value of the incidence angle. This can provide subwavelength sensitivity such that millimeter detection accuracy of ground movement has been reported with spaceborne SAR [21]–[24]. The phase maps shown in Fig. 6 can be converted to maps of Δh with (8). It is clear from the sequence of images that phase wraparound greater than -180° occurred over some of the features. Even if we just consider $\pm 180^\circ$ changes close to the center of the soil sample, (8) predicts height variations of at least ± 1.7 cm.

As the phase cannot be explained by the physical movement of the surface horizon, which was essentially static during the measurements, we have to look elsewhere for enlightenment. The effect is not an artifact of the measurement system (this is well calibrated and characterized), and it could never produce the intricate phase patterning in the imagery. The only explanation is a phase signature related to the only changing variable during the measurement program, namely, m_v. There is an understanding that reducing soil moisture leads to greater penetration into a soil volume. Ulaby *et al.* [25] has provided

an expression for the dependence of penetration depth P into a soil sample with complex dielectric constant ε

$$P = \frac{2\pi}{\lambda} \left| \mathrm{Im}[\sqrt{\varepsilon}] \right| \tag{9}$$

where λ is the free-space wavelength. Penetration is defined as the point in the medium where the signal has fallen to $1/e$ of the value at the surface of the medium. Equation (14) from [26] provides an expression to estimate the real ε_r and imaginary ε_i components of the dielectric constant at 5 GHz for a 100% sandy soil as a quadratic function of m_v

$$\varepsilon_r = 2.0 + 31.6 m_v + 106.1 m_v^2 \tag{10}$$

$$\varepsilon_i = 0.1 + 1.6 m_v + 42.1 m_v^2. \tag{11}$$

This scheme is idealistic in that it only considers the signal lost to a homogeneous medium through attenuation with no scattering losses. Equations (10) and (11) indicate that the ratio of the imaginary part to the real part of the dielectric reduces from 0.23 to 0.11 between Days 1 and 50. This is expected as the soil becomes less lossy with decreasing moisture. With the necessary inclusion of scattering losses, the penetration depth will be reduced, but the notion is still useful in defining a volume of interest. On Day 1, $m_v = 0.38$, so from (9)–(11), $P = 0.8$ cm. At the end of the experiment, $m_v = 0.10$, and $P = 3.4$ cm. This indicates that the soil return was dominated by the top few centimeters. This assumes a homogenous medium, but it is acknowledged that such a medium has no impedance discontinuities within its volume and, therefore, no ability to backscatter. Heterogeneity in some form is required to produce scattering, and the presence of a vertical moisture gradient may be the source of any volume return [27].

For a single-look image, we measure a resultant phase at a pixel, arising from a superposition of returns from all scatterers within the soil volume and surface. Between image pairs, we saw the persistence of coherent phase patterns. This indicates perseverance of the same scattering mechanism at each point over the sample between Days 1 and 37. With Day 50, both phase and amplitude coherence appear lost with the previous set of measurements, indicative that the physical changes at each pixel are so profound that we can no longer consider it as the same target—the principle of interferometric decorrelation. The question arises as to what physical change in the scene is the differential phase responding to. We expect the return at the surface to be the strongest contribution due to the large air–soil impedance discontinuity, with decreasing returns with increasing depth. The temporal sequence showed a continuous drift of the differential phase toward negative values. While it is tempting to ascribe this to increasing penetration into the soil, phase is a coherent summation of the scattered fields over the surface, within the volume and between the surface and volume. Arising as an interference phenomenon between these sources, it likely provides no deterministic measure of penetration changes.

Most importantly, whatever the exact nature of the scattering mechanism producing the differential phase, this paper has been able to demonstrate the presence of phase changes in the absence of any surface deformation, which are instead linked to soil moisture changes.

VI. Concluding Remarks

A seven-week experiment looked at the C-band differential phase behavior of a sandy nonexpansive soil in response to varying moisture content (or equivalently—from (10) and (11)—varying dielectric properties). Large phase changes were seen over the soil in the absence of any physical movement of the surface. Although the phase patterning was complex, it showed a smooth and continuous temporal development, with some features displaying changes greater than 180°. This paper has provided the first experimental confirmation of a suspected link between interferometric phase and soil moisture. It has important implications for the conventional interpretation of interferometric phase from SAR platforms, with regard to physical changes in the scene that it represents. For the DInSAR generated over regions dominated by sandy soils, it indicates the possibility of the presence of a strong soil moisture signal in the interferometric phase. Even for interferograms generated over expansive soils, the soil moisture signal may still provide a significant source of error in land deformation studies.

This paper raises the important question of whether DInSAR phase can be used as a proxy for soil moisture change mapping, a very important economic and environmental parameter. Although the work has not provided a description of the underlying scattering mechanism that produces the phase changes, the persistence of coherent phase features as the soil state changed from near saturated to damp is promising that a useful phase–moisture signal exists. The linear relationship between phase and soil moisture over the m_v range of 0.16–0.38 was found by spatially averaging over a 1.5 m $\times$ 1.5 m region. The area is representative of the resolution footprint of some current airborne and spaceborne SARs. If the behavior proves to be consistent between sandy soil types, the derived phase response of 2.6° per 1% change in soil moisture indicates a feasible measurement accuracy for soil moisture change at the level of several percent. Further work is required to confirm the wider applicability of the results to other soils, using both laboratory and field campaigns. The L-band is generally regarded as more suited to soil monitoring than the C-band, and future demonstration at this frequency would seem appropriate.

References

[1] E. T. Engman, "Microwave remote sensing of soil moisture, progress, potential and problems," in *Proc. IGARSS*, Firenze, Italy, Jul. 10–14, 1995, vol. 1, pp. 489–491.

[2] P. A. Dirmeyer, "Using a global soil wetness dataset to improve seasonal climate simulation," *J. Clim.*, vol. 13, no. 16, pp. 2900–2922, Aug. 2000.

[3] S. R. McKee, J. D. Kalma, S. W. Franks, and Y. Shao, "The relationship between temporal surface temperature trends and soil moisture status: An exploratory study with a coupled landsurface-atmosphere model," in *Proc. IGARSS*, Sydney, Australia, Jul. 10–14, 2001, vol. 3, pp. 1312–1314.

[4] F. L. Yang, A. Kumar, and K. M. Lau, "Potential predictability of U.S. summer climate with "perfect" soil moisture," *J. Hydrometeorol.*, vol. 5, no. 5, pp. 883–895, 2004.

[5] R. Grayson and G. Bloschl, *Spatial Pattern of Catchment Hydrology: Observations and Modelling*. Cambridge, U.K.: Cambridge Univ. Press, 2001.

[6] A. Beaudoin, T. Le Toan, and Q. H. J. Gwyn, "SAR observations and modeling of the C-band backscatter variability due to multiscale geometry and soil moisture," *IEEE Trans. Geosci. Remote Sens.*, vol. 28, no. 5, pp. 886–895, Sep. 1990.
[7] M. Zribi, N. Baghdadi, N. Holah, and O. Fafin, "New methodology for soil surface moisture estimation and its application to ENVISAT-ASAR multi-incidence data inversion," *Remote Sens. Environ.*, vol. 96, no. 3/4, pp. 485–496, Jun. 2005.
[8] Y. Oh, "Quantitative retrieval of soil moisture content and surface roughness from multipolarized radar observations of bare soil surfaces," *IEEE Trans. Geosci. Remote Sens.*, vol. 42, no. 3, pp. 596–601, Mar. 2004.
[9] I. Hajnsek, T. Jagdhuber, H. Schön, and K. P. Papathanassiou, "Potential of estimating soil moisture under vegetation cover by means of PolSAR," *IEEE Trans. Geosci. Remote Sens.*, vol. 47, no. 2, pp. 442–454, Feb. 2009.
[10] A. K. Gabriel, R. M. Goldstein, and H. A. Zebker, "Mapping small elevation changes over large areas: Differential radar interferometry," *J. Geophys Res.*, vol. 94, no. B7, pp. 9183–9191, 1989.
[11] D. Massonnet, T. Holzer, and H. Vadon, "Land subsidence caused by the East Mesa geothermal field, California, observed using SAR interferometry," *Geophys. Res. Lett.*, vol. 24, no. 8, pp. 901–904, 1997.
[12] H. A. Zebker, P. Rosen, and R. Goldstein, "On the derivation of coseismic displacement fields using differential radar interferometry: The Landers earthquake," *J. Geophys. Res.*, vol. 99, no. B10, pp. 19617–19634, 1994.
[13] G. Peltzer and P. Rosen, "Surface displacement of the 17 May 1993 Eureka Valley, California, earthquake observed by SAR interferometry," *Science*, vol. 268, no. 5215, pp. 1333–1336, 1995.
[14] M. Nolan, D. R. Fatland, and L. Hinzman, "DInSAR measurement of soil moisture," *IEEE Trans. Geosci. Remote Sens.*, vol. 41, no. 12, pp. 2802–2813, Dec. 2003.
[15] M. Nolan and D. R. Fatland, "Penetration depth as a DInSAR observable and proxy for soil moisture," *IEEE Trans. Geosci. Remote Sens.*, vol. 41, no. 3, pp. 532–537, Mar. 2003.
[16] K. Morrison, J. C. Bennett, G. Cookmartin, A. J. McDonald, and S. Quegan, "Three-dimensional X-band SAR imaging of a small conifer tree," *Int. J. Remote Sens.*, vol. 22, no. 4, pp. 705–710, 2001.
[17] K. Sarabandi, F. T. Ulaby, and M. Ali Tassoudji, "Calibration of polarimetric radar systems with good polarization isolation," *IEEE Trans. Geosci. Remote Sens.*, vol. 28, no. 1, pp. 70–75, Jan. 1990.
[18] W. Goodman, *Introduction to Fourier Optics*. New York: McGraw-Hill, 1968.
[19] J. C. Bennett, K. Morrison, A. M. Race, G. Cookmartin, and S. Quegan, "The UK NERC fully portable polarimetric ground-based synthetic aperture radar (GB-SAR)," in *Proc. IGARSS*, Honolulu, HI, Jul. 24–28, 2000, vol. 5, pp. 2313–2315.
[20] K. Morrison, G. Cookmartin, J. C. Bennett, S. Quegan, and A. Race, "Polarimetric calibration strategy for long-duration imaging with a ground-based SAR," *Can. J. Remote Sens.*, vol. 31, no. 1, pp. 1–6, Feb. 2005.
[21] A. Ferretti, C. Prati, and F. Rocca, "Permanent scatterers in SAR interferometry," *IEEE Trans. Geosci. Remote Sens.*, vol. 39, no. 1, pp. 8–20, Jan. 2001.
[22] C. Prati, F. Rocca, and A. Monti Guarnieri, "SAR interferometry experiments with ERS-1," in *Proc. 1st ERS-1 Symp.*, Cannes, France, Nov. 4–6, 1992, pp. 211–218.
[23] C. Colesanti, A. Ferretti, C. Prati, and F. Rocca, "Multi-image satellite SAR interferometry: State of the art and future trends," in *Proc Radar Conf.*, Adelaide, Australia, Sep. 3–5, 2003, pp. 239–244.
[24] A. Ferretti, G. Savio, R. Barzaghi, A. Borghi, S. Musazzi, F. Novali, C. Prati, and F. Rocca, "Submillimeter accuracy of InSAR time series: Experimental validation," *IEEE Trans. Geosci. Remote Sens.*, vol. 45, no. 5, pp. 1142–1153, May 2007.
[25] F. T. Ulaby, R. K. Moore, and A. K. Fung, *Microwave Remote Sensing: Volume II*. Reading, MA: Addison-Wesley, 1982, p. 847.
[26] M. T. Hallikainen, F. T. Ulaby, M. C. Dobson, and M. A. El-Rayes, "Microwave dielectric behavior of wet soil—Part 1: Empirical models and experimental observations," *IEEE Trans. Geosci. Remote Sens.*, vol. GRS-23, no. 1, pp. 25–34, Jan. 1985.
[27] B. Rabus, H. Wehn, and M. Nolan, "The importance of soil moisture and soil structure for InSAR phase and backscatter, as determined by FDTD modeling," *IEEE Trans. Geosci. Remote Sens.*, vol. 48, no. 5, pp. 2421–2429, May 2010.

Keith Morrison (M'97) received the B.Sc. degree in physics with astrophysics from the University of Leicester, Leicester, U.K., in 1983, and the Ph.D. degree in astronomy and astrophysics from the University of St. Andrews, St. Andrews, U.K., in 1987.

He was with the British Antarctic Survey in 1987–1994, with Sheffield University, Sheffield, U.K., in 1994–2000, and with QinetiQ Malvern in 2000–2002. Since 2002, he has been with Cranfield University, Shrivenham, U.K. His main research interest is the development and application of ground-based SAR imaging applied to environmental remote sensing.

John C. Bennett received the B.Eng. and Ph.D. degrees in electronic engineering from the University of Sheffield, Sheffield, U.K., in 1970 and 1974, respectively.

At present, he is a consultant, having retired from his post as a Reader at the University of Sheffield. He is currently involved in the use of both laboratory and outdoor ground-based SAR systems for RCS measurements. He has previously been involved with the microwave metrology of reflector antennas and antenna near-field/far-field transformation techniques.

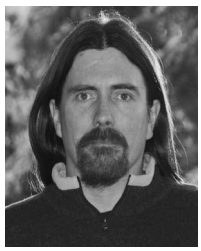

Matt Nolan received the B.S. degree in mechanical engineering from Carnegie Mellon, Pittsburgh, PA, in 1988, the M.S. degree in arctic engineering from the University of Alaska at Anchorage, Anchorage, in 1992, and the Ph.D. degree in geophysics from the University of Alaska at Fairbanks, Fairbanks, in 1998.

He is currently a Research Associate Professor with the University of Alaska at Fairbanks. His primary research interests include glaciers, permafrost, and climate in the Arctic, using field and remote sensing techniques.

Raghav Menon received the B.E. degree in electronic and instrumentation engineering from the Government College of Technology, Coimbatore, India, in 2001, and the M.Sc. degree in communications and signal processing from the University of Newcastle, Newcastle upon Tyne, U.K., in 2003.

He is currently a Research Fellow with Cranfield University, Shrivenham, U.K., with interests in target recognition, imaging radars and sonars, and array signal processing.